Journal of Materials Chemistry A

Enhancement of Catalytic Performance by Controlling the Type of Junctions in Metal/Oxide Catalysts for Urea Oxidation Reaction

Journal:	*Journal of Materials Chemistry A*
Manuscript ID	TA-ART-03-2025-001847.R1
Article Type:	Paper
Date Submitted by the Author:	31-May-2025
Complete List of Authors:	Cha, Yoo Lim; Auburn University, Materials Engineering Wu, Shuai; Auburn University, Materials Engineering Bijoy, Md Sabbir Hossen; Auburn University, Materials Engineering Taghavi Kouzehkanan, Seyed Morteza; Auburn University, Chemical Engineering Kim, Wonhyeong; Auburn University, Materials Engineering Chen, Pengyu; Auburn University, Materials Engineering Oh, Tae-Sik; Auburn University, Chemical Engineering Kargar, Fariborz; Auburn University, Department of Electrical and Computer Engineering Kim, Sun Hee; Incheon National University, Department of Fashion Industry Kim, Dong-Joo; Auburn University, Materials Engineering

Paper

Enhancement of Catalytic Performance by Controlling the Type of Junctions in Metal/Oxide Catalysts for Urea Oxidation Reaction

Received 00th January 20xx,
Accepted 00th January 20xx

DOI: 10.1039/x0xx00000x

Yoo Lim Cha,[a] Shuai Wu,[a] Md Sabbir Hossen Bijoy,[a] Seyed Morteza Taghavi Kouzehkanan,[b] Wonhyeong Kim,[a] Pengyu Chen,[a] Tae-Sik Oh,[b] Fariborz Kargar,[a] Sun Hee Kim*[c] and Dong-Joo Kim*[a]

The urea oxidation reaction (UOR) is a vital process for both hydrogen fuel production and the treatment of environmental contaminants. Metal/oxide catalysts, widely used not only in UOR but also in various other catalytic processes, are highly regarded for their ability to enhance catalytic performance by increasing surface area and utilizing strong metal-support interactions (SMSI). Despite their extensive use, the role of electronic properties at the metal/oxide interface, particularly the influence of junction type (Ohmic vs. Schottky), has not been thoroughly investigated. This study aims to address this gap by examining the impact of junction type on the catalytic performance of metal/oxide systems in UOR. Ni/ZnO systems with varying Ga doping concentrations (0–10 at.% Ga) on the ZnO were synthesized to modulate the junction type between Ohmic and Schottky. Comprehensive analyses revealed a transition from Schottky to Ohmic junctions at 2 at.% Ga, followed by a return to Schottky behavior at 8 at.% Ga. Ga-doped ZnO with Ohmic junctions, (i.e., 2 at.% and 4 at.%) exhibited significantly higher catalytic activity, generating higher current at lower overpotentials compared to systems with Schottky junctions (undoped ZnO, and Ga(8–10 at.%)-doped ZnO), This enhancement is attributed to the formation of oxidative strong metal-support interaction (O-SMSI). Furthermore, Ohmic junction systems demonstrated improved electrochemical durability due to the inherently low interfacial resistance. These findings highlight the critical role of junction type in optimizing the performance of metal/oxide catalysts for UOR and provide valuable insights for the rational design of more efficient catalytic systems.

1. Introduction

Urea oxidation has garnered significant research interest owing to its remarkable efficiency in producing high-purity hydrogen fuel while simultaneously decomposing environmental contaminants. Notable examples of urea oxidation catalysts include noble metals like Pt, Pd, Rh, Ru, and Au, and transition metals such as Ni, Co, and Fe, along with metal oxides like SnO_2, ZnO, TiO_2, SiO_2, and Al_2O_3, which function as semiconductors. Numerous studies aim to optimize catalyst design to maximize reactant conversion and product selectivity.[1–8] However, single-component catalysts face limitations due to the Brønsted–Evans–Polanyi (BEP) relation, which links activation energy to reaction enthalpy, creating a trade-off between activity and selectivity.[9] These constraints can be addressed by employing multi-component composite catalysts.[10] A representative example of multi-component composite catalysts is the metal/oxide system, also known as supported metal catalysts, where metal particles are dispersed on high-surface-area oxides. While the metal acts as the active phase, the oxide serves as a support that enhances surface area, stability, and forms metal–oxide interfaces. These interfaces play a key role in modulating catalytic activity and selectivity through metal–support interactions (MSI), which alter the catalyst's electrochemical behavior. Building on these advantages, numerous studies have investigated metal–oxide catalysts as promising candidates for urea oxidation. For example, Basumatary et al. developed Ni-Cu/ZnO@multi-walled carbon nanotubes (MWCNT) composites for direct urea fuel cell (DUFC) anode catalysts, achieving 1.21 and 6 times higher current density generation than Ni-Cu/MWCNT and ZnO/MWCNT catalysts, respectively, due to the increased specific surface area contributed by the ZnO.[7] Yoon et al. developed an Ag-coated nanorod-shaped ZnO on carbon paper (CP) for non-enzymatic urea detection, demonstrating 2.3, 4.9, and 450 times higher current density than ZnO/CP, Ag/CP, and CP, respectively.[11,12] This enhanced performance was attributed to the larger surface area of the nanorods and the formation of Ohmic junctions, enabled by the higher work function of Ag compared to ZnO.

While these studies demonstrate the enhanced performance of metal/oxide catalysts in urea oxidation, many attribute this improvement to so-called 'synergistic effects'—a term that often lacks clarity regarding the underlying mechanisms. Consequently, substantial research efforts have focused on unveiling how metal/oxide combinations surpass the activity of single-component materials, leading to the proposal of various

[a] Materials Research and Education Center, Auburn University, Auburn, AL 36849, USA.
[b] Department of Chemical Engineering, Auburn University, Auburn, AL 36849, USA.
[c] Department of Fashion Industry, Incheon University, Incheon 22012, Korea.
† Electronic supplementary information (ESI) available. See DOI: 10.1039/x0xx00000x

mechanisms such as strong metal–support interaction (SMSI), charge-transfer effects, dual-site catalysis, structural promotion, the presence of interface-specific active sites, oxygen vacancies, and Lewis acid sites. The electronic effect at metal–oxide interfaces, caused by the alignment of their Fermi levels, is one of the most fundamental and universal factors influencing their behavior. This alignment leads to charge transfer between the metal and oxide, regardless of the specific reaction, material, or synthesis method. Depending on how the energy levels match, the interface can form either an Ohmic contact, which allows easy, bidirectional charge flow with low resistance, or a Schottky contact, which introduces a barrier that restricts charge movement to one direction. These contact types significantly affect how charge is transferred and distributed at the interface, ultimately playing a key role in the electrocatalytic performance of metal–oxide systems.[13] Reflecting this, many recent studies on metal/oxide electrocatalysts have emphasized the junction type—particularly the formation of Ohmic contact—as a key factor responsible for the catalyst's superior performance.[14,15] However, it is not easy to form Ohmic contacts in all metal/oxide catalysts because metals generally have higher work functions than semiconductors, which increases the probability of forming Schottky contacts. Also, in catalyst research, metals with higher work functions are predominantly used due to their higher catalytic efficiency. Therefore, metal/oxide catalysts are more likely to possess Schottky junctions than Ohmic junctions. Nevertheless, the extent to which the electrochemical performance of metal/oxide catalysts differs between Ohmic and Schottky contacts has not been quantitatively described. In addition, few studies have investigated which specific material properties of the oxide influence overall catalytic performance, particularly under conditions where the metal/oxide interface forms either an Ohmic or Schottky contact. Understanding these differences could provide valuable insights for the rational design of future catalysts.

Therefore, here we report a systematic model study aimed at understanding how the type of electronic junction—Ohmic or Schottky—formed at the metal/oxide interface affects catalytic performance, and which specific properties of the oxide are most critical for optimizing catalyst design under each junction condition. For this model study, Ni metal with a work function value of 5.01 eV[16–18], was employed due to its widespread use in UOR.[19,20] Additionally, ZnO was selected as the oxide support, as it offers tunable electron affinity values ranging from 4.5 to 5.0 eV[21–23] and has also been extensively studied as a support material for UOR[7,12,23,24], making it a suitable candidate for this investigation.

To modulate the type of junction at the Ni/ZnO interface, a small amount of an n-type dopant was introduced to tailor the electronic band structure of ZnO. Among group XIII dopants, Ga^{3+} was chosen based on its reported structural promotion effects in Cu/ZnO catalysts, along with its ability to enhance conductivity, reduce resistivity, and improve electron mobility due to its covalent bond length being similar to that of Zn–O.[25–28] To isolate the effect of the junction type, we adopted a well-established Ga-doped ZnO synthesis method from the literature to ensure consistency across samples. Following prior studies, the Ga doping concentration was varied from 0 to 10 at.%, encompassing the range in which the maximum effective doping level is typically observed.[29,30] By conducting a thorough analysis of ZnO and Ga-doped ZnO before and after nickel loading—from chemical, optical, electrical, and electrochemical perspectives—we aimed to gain insights into the importance of the type of junctions formed in heterogeneous catalysts and how the oxide's properties, under each junction type, influence catalyst performance.

2. Experimental

2.1 Materials

Zinc acetate dihydrate ($Zn(CH_3COO)_2H_2O$) and gallium nitrate hydrate ($Ga(NO_3)_3{\cdot}xH_2O$) were used as the zinc and gallium sources, respectively. Ammonia solution (NH_4OH, 25%) was added as a complexing agent to form zinc hydroxide ($Zn(OH)_2$), a white precipitate precursor to ZnO. For nickel deposition, nickel(II) nitrate hexahydrate ($Ni(NO_3)_2{\cdot}6H_2O$) was used as the nickel precursor. Ethylene glycol ($(CH_2OH)_2$), hydrazine monohydrate (N_2H_4 64–65 %), and sodium hydroxide (NaOH) served as the solvent, reducing agent, and pH adjustment source, respectively. All reagents were purchased from Sigma Aldrich and used as received without further purification. Deionized water (18 $M{\cdot}cm^{-1}$) was used for all experiments.

2.2 Preparation of a ZO and GZO

Zinc oxide (ZO) and gallium-doped zinc oxide (GZO) were synthesized via a hydrothermal method. For ZO synthesis, 5 mM of zinc acetate dihydrate was dissolved in 25 mL of deionized (DI) water, followed by the dropwise addition of 3 mL of 5 M ammonia solution under stirring. After stirring for 5 minutes, the solution was transferred to a 50 ml Teflon-lined stainless-steel autoclave and heated at 90 °C for 5 hours. After cooling to room temperature, the synthesized ZnO nanopowder was washed repeatedly with DI water until a neutral pH was reached and collected via centrifugation. The final product was dried at 80 °C for 6 hours in an oven.

To synthesize GZO, the total metal source precursor was fixed at 5 mM, while the molar ratio of zinc acetate dihydrate to gallium nitrate hydrate was varied. The gallium content was adjusted in increments from 2 to 10 mol.%. Based on the atomic percentage of Ga, the samples were denoted as Ga 2 at.%-doped ZnO, Ga 4 at.%-doped ZnO, Ga 6 at.%-doped ZnO, Ga 8 at.%-doped ZnO, and Ga 10 at.%-doped ZnO, abbreviated as G2ZO, G4ZO, G6ZO, G8ZO, and G10ZO, respectively. The weighed zinc and gallium precursors were dissolved in 25 mL of DI water under stirring, and the same procedure as for ZO synthesis was followed.

2.3 Ni nanoparticle deposition upon ZO and GZO

Ni/ZO and Ni/GZO metal-semiconductor composites were synthesized by depositing Ni nanoparticles onto the

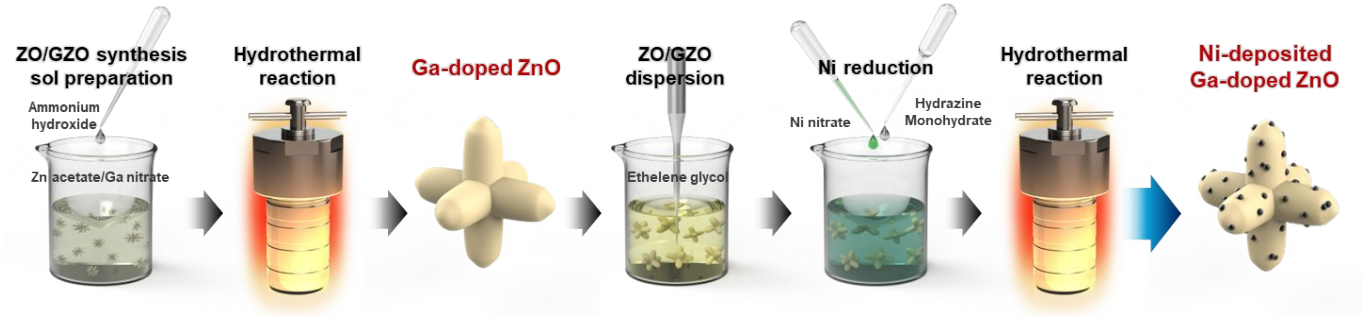

Scheme. 1 Synthesis process for Ni/ZO and Ni/GZO.

as-prepared ZO and GZO substrates via a hydrothermal chemical reduction method.

Initially, 1 mM of the ZO or GZO powders was weighed and mixed with 2 mL of 0.17 M nickel nitrate hexahydrate aqueous solution and 28 mL of ethylene glycol, followed by sonication for 1 hour to ensure even distribution of Ni ions on the oxide surfaces. Subsequently, 50 µl of hydrazine monohydrate and 2 ml of 2 M NaOH solution were added to adjust the pH to 10–11 under continuous stirring. After 5 minutes of stirring, the mixture was transferred to a 50 ml Teflon-lined stainless-steel autoclave and heated at 160 °C for 6 hours. After cooling to room temperature, the resulting Ni/ZO and Ni/GZO nanocomposites were washed five times with DI water and collected via centrifugation. The powders were then dried in a vacuum oven at 60 °C for 12 hours. For comparison, pure Ni nanoparticles were synthesized using the same procedure without adding ZO or GZO powders. A schematic diagram of the synthesis steps for ZO, GZO, and Ni deposition is shown in Scheme 1.

2.4 Catalysts Characterization

The catalysts' crystalline structures were analyzed through X-ray diffraction (XRD), employing a Cu Kα radiation source (λ = 1.5406 Å) within the 2θ range of 10–90° on a D8 Discover instrument (Bruker), operating at a generator voltage of 40 kV and a current of 40 mA. Surface morphologies and elemental compositions were assessed using field emission scanning electron microscopy (FESEM) on a JBM-7000F instrument (JEOL), coupled with energy dispersive X-ray spectroscopy (EDX). The specific surface area (SSA) was determined through Brunauer-Emmet-Teller (BET) analysis, involving nitrogen adsorption-desorption measurements at 77 K on a NOVA 2200e instrument (Quantachrome). Further chemical compositions and oxidation states of the elements were ascertained via X-ray photoelectron spectroscopy (XPS) using a K-alpha instrument (Thermo U.K.) equipped with a monochromatic Al Kα radiation source (hν = 1486.6 eV), calibrated with respect to the binding energy of C 1s (284.8 eV). UV-visible diffuse reflectance spectroscopy (DRS) was performed using a Cary 5000 UV/VIS/NIR spectrophotometer to investigate the optical properties of the catalysts. The oxide powders were uniaxially pressed into cylindrical pellets (10 mm in diameter and 1 mm thick) under a pressure of 4–5 tons. To enhance the mechanical strength and interparticle connectivity, the pellets were sintered in air at 1000 °C for 2 hours. After sintering, one half of one side of each pellet was coated with Ni paste, which was then cured at 65 °C for 30 min. The resulting Ni-deposited ZO/GZO pellets were assembled into a three-electrode electrochemical system and subjected to the urea oxidation reaction (UOR). Subsequently, in situ Raman spectroscopy was performed to investigate the formation of strong metal–support interactions (SMSI). Raman spectra were collected from both the oxide and Ni surfaces using a Renishaw inVia Raman microscope equipped with a 532 nm excitation laser and a 10 s exposure time.

To determine the type of electronic junction formed between Ni and ZO/GZO, one side of each pellet was coated with nickel paste and the other with silver paste as opposing electrodes. The coatings were cured at 65 °C (Ni) and 200 °C (Ag) for 30 minutes to ensure stable electrical contact. Current–voltage (I–V) characteristics were measured using a source meter (Keithley 2400) in a two-electrode configuration, with the voltage swept from –0.5 to +3.0 V at room temperature.

2.5 Electrochemical Test

Electrochemical assessments were conducted using the SP-200 electrochemical workstation (Potentiostat, BioLogic, France). A standard three-electrode setup was employed for the urea oxidation reaction (UOR) evaluation, with a 3M Ag/AgCl electrode serving as the reference electrode and a platinum wire as the counter electrode. Working electrodes were prepared by modifying carbon paper (CP) with the synthesized catalysts. The catalyst ink was prepared by ultrasonication of the powder samples (5 mg) with 10 µL Nafion solution (5 wt.%), 200 µL of ethanol, and 50 µL DI water solution for 30 minutes. Then, 5 µL of the catalyst ink was drop-cast onto the CP with dimensions of 0.5 × 1.0 cm^2 and dried at 75 °C for 5 minutes. Potentials were calibrated to the reversible hydrogen electrode (RHE) using the equation E (V vs. RHE) = 0.197V + E (V vs Ag/AgCl) + 0.059 pH. Polarization curves were recorded in a solution containing 1.0 M KOH and 0.5 M urea solution using linear sweep voltammetry (LSV) with a scan rate of 5 mV s^{-1}.

3. Results and discussion

3.1 Materials Analysis

The crystal structures of the ZO and GZO (2–10 at.%) were analyzed by XRD. All samples showed diffraction peaks corresponding to the hexagonal wurtzite ZnO structure (JCPDS

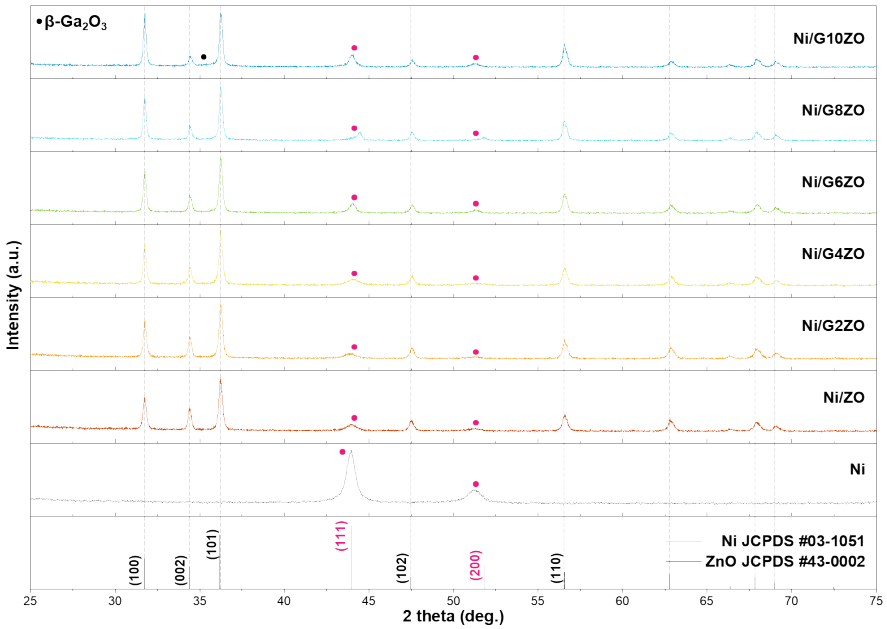

Fig. 1 XRD patterns of Ni/ZO and Ni/GZO (Ga 2, 4, 6, 8, and 10 at.%).

43-0002), with the (101) plane being the most intense, indicating high crystallinity (Fig. S1). As the Ga content increased from 0 to 2 at.%, peak shifts toward higher 2Θ values were observed, suggesting lattice contraction due to substitution of larger Zn^{2+} ions (0.74 Å) by smaller Ga^{3+} ions (0.62 Å) (Fig. S2).[31] However, at 4–6 at.% Ga, the lattice expanded due to Ga^{3+} occupying the interstitial sites (Table S1).[32] At 8 at.%, the appearance of a secondary phase (β-Ga_2O_3) caused a slight lattice contraction.

Morphological evolution was investigated using FE-SEM (Fig. S3). Undoped ZO exhibited a flower-like morphology formed by randomly oriented nanorods. This is attributed to the spontaneous growth of multiple axes due to internal defects and the absence of additives like HMTA, which typically direct vertical growth along the [001] axis.[33–35] With 2–4 at.% Ga, the flower-like structure persisted, but rod tips became rounder. At higher doping levels (6–10 at.%), the particles transitioned to the rod-like morphologies with increased length and diameter, indicating enhanced growth along the c-axis.[36]

This morphological transformation can be explained by the electronic and structural role of Ga^{3+} dopants. Substitution of Zn^{2+} by Ga^{3+} increases the surface charge, promoting oxygen ion adsorption and accelerating vertical growth. At the same time, the introduction of Ga increases the energy barrier for ZnO nucleation, reducing the number of heterogeneous nucleation sites. Additionally, Ga precursors in the solution may form complexes with OH^- ions, lowering the effective OH^- concentration and slowing down the Zn^{2+}–OH^- reaction kinetics.[36] These combined effects suppress vertical nucleation while promoting lateral crystal growth, leading to an overall increase in rod diameter. Together, these effects result in longer and thicker nanorods as the Ga doping level increases.

As a result of these structural and chemical effects, the synthesized GZO samples exhibited uniform elemental distribution. EDS mapping (Fig. S4) confirmed that Zn, Ga, and O were evenly dispersed in G2ZO, and similar homogeneity was observed across other compositions. Furthermore, EDS point analysis (Table S2) showed that the measured elemental ratios closely matched the nominal doping levels, indicating successful and controlled incorporation of Ga^{3+} into the ZnO lattice.

To investigate the role of the oxide layer in supporting metal catalysts, Ni was deposited onto the as-synthesized ZO and GZO samples via chemical reduction. XRD analysis (Fig. 1) confirmed that the hexagonal ZnO structure remained intact after Ni loading, with consistent peak shifts and secondary phase trends across all compositions. Two additional peaks at 43.95° and 51.24° in 2θ, corresponding to FCC Ni (JCPDS #03-1051), indicated successful reduction of Ni^{2+} to metallic Ni, with negligible oxidation products.

SEM and EDS analyses (Fig. 2) further verified that Ni nanoparticles (100–250 nm) were uniformly deposited on the oxide surfaces. In particular, the rod-like morphology of the ZnO-based supports facilitated preferential deposition along the (100) sidewalls, which are the most exposed facets. Elemental mapping confirmed homogeneous Ni distribution without aggregation, highlighting the structural compatibility between the Ni and the GZO support.

3.2 Electronic Band Structure Analysis

To examine how Ga doping affects the electronic band structure of ZnO, UV–Vis diffuse reflectance spectroscopy (DRS), and XPS valence band analysis were conducted. Fig. S6(a) shows the UV–Vis DRS spectra of ZO and GZO, featuring strong and broad absorption bands between 300–400 nm, which are attributed to intrinsic $O_{2p} \rightarrow Zn_{3d}$ electron transitions from the valence to conduction band—a hallmark of ZnO's optical behavior.[37,38] As Ga content increased, a red shift was observed up to G6ZO, indicating band gap narrowing due to Ga-induced shallow states.[31] From G8ZO onward, a blue shift was observed, attributed to the formation of a secondary phase, β-Ga_2O_3,

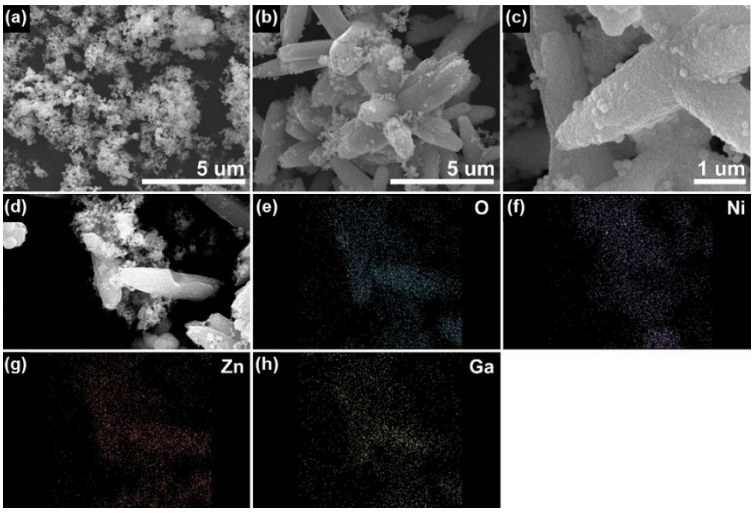

Fig. 2 SEM image of (a) Ni and (b, c) Ni-deposited Ga(2 at.%)-doped ZnO, and (d–h) EDS mapping of Ni-deposited Ga(2 at.%)-doped ZnO.

which has an ultra-wide band gap (4.7–4.9 eV). The calculated optical band gaps (Fig. S6(b), Table S3) aligned with these observations.[39,40] XPS valence band spectra (Fig. S7) were used to determine the valence band maxima of each oxide sample. Using this data along with the known work function of Ni (5.01 eV), the Schottky barrier heights (E_{SBH}) at the Ni/oxide interface were estimated (Table S3).[16–18] The calculations suggested that only Ni/G2ZO and Ni/G4ZO are likely to form Ohmic junctions, while the others exhibit Schottky-type behavior (Fig. 3). To verify these predictions, Ni 2p XPS spectra before and after composite formation were analyzed (Fig. S8). Deconvoluted peaks indicated the presence of metallic Ni, NiO (Ni^{2+}), and Ni_2O_3 (Ni^{3+}).[41] For Ni/G2ZO, G4ZO, and G6ZO, the Ni^{2+} $2p_{3/2}$ peak exhibited a positive shift relative to pristine Ni, indicating electron transfer from Ni to the oxide. This supports the formation of Ohmic junctions and is characteristic of oxidative strong metal–support interaction (O-SMSI), where Ni becomes partially positively charged.[42]

In contrast, Ni/ZO, G8ZO, and G10ZO exhibited negligible or negative shifts in the Ni^{2+} $2p_{3/2}$ peak, indicating increased electron density on Ni due to electron transfer from the oxide to the metal. This behavior is consistent with reductive strong metal–support interaction (R-SMSI), in which the metal acquires a negative charge, forming a Schottky-type contact.[43]

To confirm the formation of O-/R-SMSI, ex-situ Raman spectroscopy was measured on both the oxide and metal surfaces after UOR conditions (Fig. S10). As shown in Fig. S11(a), the A_1(LO) peak intensity at 583.9 cm^{-1} increased with Ga doping and reached a maximum at G8ZO, indicating elevated surface electron density and oxygen vacancy concentration—consistent with the formation of a negatively charged oxide under R-SMSI conditions.[44] In contrast, G2ZO and G4ZO showed suppressed A_1(LO) intensity, suggesting electron depletion at the oxide surface, in line with the electron transfer from Ni to the oxide observed in O-SMSI. Additionally, Fig. S11(b) shows the corresponding Raman intensity of urea-derived anionic intermediates (e.g., CO_3^{2-} and OCN^-) adsorbed at 1004.16 and 1064.89 cm^{-1}.[45,46] The strongest signals were observed for Ni/G2ZO and Ni/G4ZO, confirming enhanced adsorption of negatively charged intermediates onto positively polarized Ni surfaces formed via O-SMSI. The weaker signals in Ni/G8ZO and Ni/G10ZO indicate that Ni in these systems is more electron-rich and therefore less favorable for anionic adsorption, which is consistent with R-SMSI behavior.

Interestingly, despite the band alignment for Ni/G6ZO suggesting a Schottky junction, XPS evidence of electron transfer points to Ohmic-like behavior. This discrepancy is attributed to possible error margins (±0.13 eV) in the valence band energy estimation from XPS. These types of junctions are also confirmed through I-V curve behavior of each oxide (Fig. S12). Overall, these results confirm that the junction type at the Ni/oxide interface can be effectively tuned through Ga doping: Ni/G2ZO, Ni/G4ZO, and Ni/G6ZO form Ohmic junctions, while Ni/ZO, Ni/G8ZO, and Ni/G10ZO form Schottky junctions.

Similar to our findings, other studies have reported a gradual transition in junction type depending on dopant concentration. For example, Suzuki et al. investigated P-doped homoepitaxial diamond in contact with various metals such as Ni, Pt, Al, and Ti. By adjusting the phosphine (P source) concentration, they controlled the P doping levels. As the P dopant concentration increased from 1.6×10^{16} to $3.0 \times 10^{19} cm^{-3}$, the electrical behavior of the Ni/P-doped diamond junction changed gradually—from strong rectifying behavior with high knee voltage(V_K) to weak rectifying behavior with lower V_K, and eventually to Ohmic contact formation.[47]

A similar trend was also observed in Al-doped ZnO systems. As the Al doping concentration increased from 1 to 5 mol%, the V_K of the metal–ZnO junction decreased from 4.25 V to values as low as 2.33 V. This indicates that higher doping levels reduce the barrier height, making it easier to form Ohmic contacts.[48]

These examples demonstrate that junction type can indeed be tuned by controlling dopant concentration—consistent with our results. The impact of this junction modulation on electrocatalytic performance is discussed in the following section.

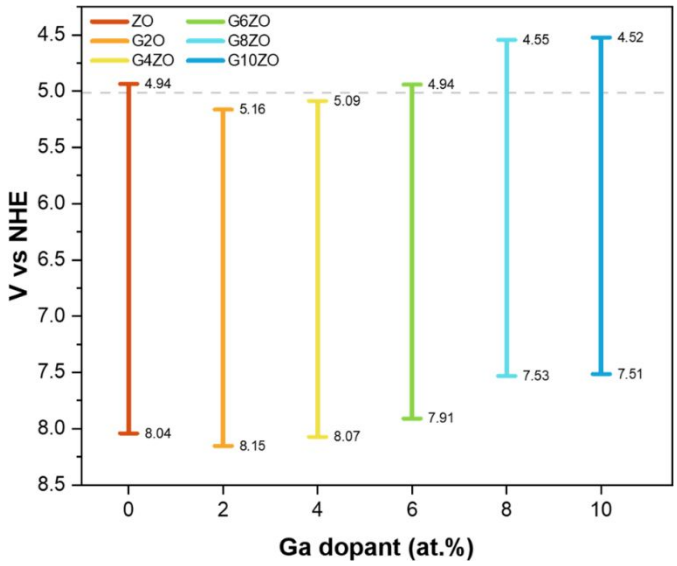

Fig. 3 Schematic diagram of ZO, GZO, and Ni work function (dotted gray line).

3.3 Electrochemical Analysis

The electrocatalytic performance of bare ZO and Ga-doped ZnO (GZO) was first evaluated under both oxygen evolution reaction (OER) and urea oxidation reaction (UOR) conditions using linear sweep voltammetry (LSV). As shown in Fig. S13(a), the G2ZO catalyst (2 at.% Ga) exhibited a significantly higher current density under UOR conditions, requiring only 1.477 V (vs. RHE) to reach 10 mA mg^{-1}—much lower than the 1.616 V needed under OER conditions. This result confirms that Ga-doped ZnO can effectively lower the energy required for hydrogen production when urea is present.

To explore how Ga doping affects catalytic activity, we compared the total charge generated during UOR (integrated from LSV curves in Fig. 4(a), Table S4). G2ZO generated the highest charge, while further increases in Ga content led to a decline. In particular, the formation of a secondary β-Ga_2O_3 phase at 8 at.% Ga resulted in a sharp decrease in current and increased overpotential. This likely stems from the formation of a resistive n–n junction between GZO and β-Ga_2O_3, which hinders charge transfer.[49,50]

Next, Ni was deposited on ZO and GZO to form metal/oxide composite catalysts, and their UOR performance was assessed. Interestingly, the activity trend of Ni/ZO and Ni/GZO differed from that of the bare oxides, suggesting that other factors, especially the type of junction at the metal/oxide interface, play a dominant role. Based on prior optimization (Fig. S13(b)), all Ni/oxide composites were synthesized with a fixed oxide-to-Ni mass ratio of 3, ensuring direct comparability across different doping levels. Among them, Ni/G2ZO showed the best performance, achieving the lowest overpotentials and the highest charge generation (5712.2 C g^{-1}), followed by Ni/G4ZO and Ni/G6ZO (Fig. 4(d, e)). These three catalysts, forming Ohmic junctions, clearly outperformed Schottky junction systems such as Ni/ZO, Ni/G8ZO, and Ni/G10ZO.

The Tafel slope analysis (Fig. 4f) further supported this distinction: Ni/G2ZO (182 mV dec^{-1}), Ni/G4ZO (148 mV dec^{-1}), and Ni/G6ZO (184 mV dec^{-1}) exhibited lower slopes—indicating faster reaction kinetics—than Ni/ZO (886 mV dec^{-1}), Ni/G8ZO (188 mV dec^{-1}), and Ni/G10ZO (197 mV dec^{-1}). This trend was also confirmed by electrochemical impedance spectroscopy (EIS), which provides insight into interfacial charge transfer resistance. According to the equivalent RC circuit model, the solution resistance (R_S) is obtained from the x-axis intercept, while the charge transfer resistance (R_{CT}) corresponds to the semicircle's radius. As shown in Fig. 4(g), the Ohmic junction systems—Ni/G2ZO (804.1 Ω), Ni/G4ZO (1028.3 Ω), and Ni/G6ZO (1030.1 Ω)—exhibited significantly lower R_{CT} values than the Schottky junction systems—Ni/G8ZO (1072.2 Ω), Ni/G10ZO (1279.5 Ω), and Ni/ZO (1880.3 Ω). These results demonstrate that Ohmic junctions promote more efficient interfacial electron transfer, further enhancing overall reaction kinetics.

This trend was further supported by the double-layer capacitance (C_{dl}) values obtained from cyclic voltammetry (CV), which reflect the electrochemically active surface area (ECSA) of each catalyst (Fig. 4h, Fig. S14). The Ohmic junction systems showed larger C_{dl} values: Ni/G6ZO (7.87 mF mg_{Ni}^{-1}), Ni/G4ZO (7.32 mF mg_{Ni}^{-1}), and Ni/G2ZO (6.5 mF mg_{Ni}^{-1}), indicating more available active sites. In contrast, Schottky junction systems exhibited lower capacitance: Ni/G8ZO (7.54 mF mg_{Ni}^{-1}), Ni/G10ZO (4.47 mF mg_{Ni}^{-1}), and Ni/ZO (3.79 mF mg_{Ni}^{-1}). These results highlight that Ohmic junctions not only reduce interfacial resistance but also provide a larger electrochemically active surface area. The combination of improved charge transfer and increased active site availability directly contributes to the enhanced electrocatalytic performance observed in these systems.

The enhanced catalytic performance of metal–oxide catalysts with Ohmic junctions can be attributed to oxidative strong metal–support interaction (O-SMSI), where electrons transfer from the Ni metal to the oxide. This electron movement results in a positively charged Ni surface and a negatively charged oxide surface, which can significantly influence intermediate adsorption during the urea oxidation reaction (UOR). For

instance, negatively charged intermediates such as CO tend to bind more effectively to the positively charged Ni, while an Ohmic junction that enables effective electron transfer from the metal to the oxide is significantly more beneficial for

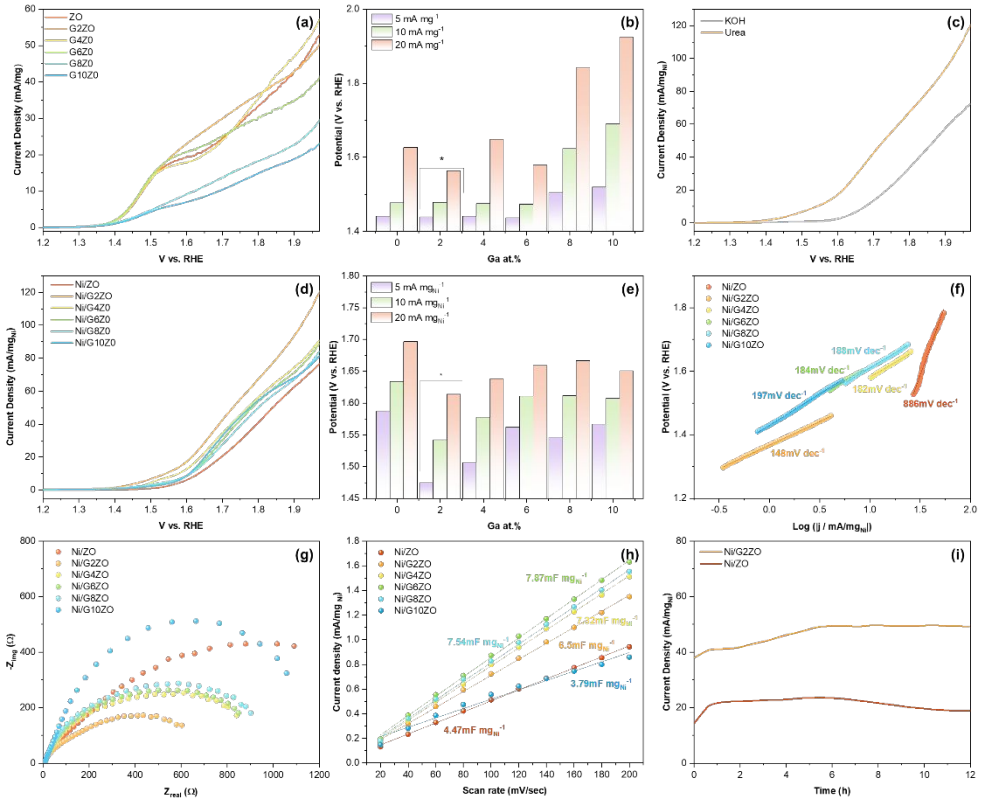

Fig. 4 Electrocatalytic UOR performances of ZO, GZO, Ni/ZO, and Ni/GZO catalysts. (a) LSV curves of ZO and GZO in UOR condition, (b) their corresponding potential acquired to achieve a current density of 5, 10, and 20 mA mg^{-1}, (c) LSV curves of Ni/G2ZO in UOR and OER conditions, (d) LSV curves of Ni/ZO and Ni/GZO in UOR condition, (e) their corresponding potential acquired to achieve a current density of 5, 10, and 20 mA mg^{-1}, (f) Tafel slopes, (g) Nyquist plot, and (h) C_{dl} values of Ni/ZO and Ni/GZO, and (i) chronoamperometry (CA) curves of Ni/G2ZO and Ni/ZO in UOR condition.

positively charged NH-containing species favor adsorption on the negatively charged oxide. This dual-site interaction is believed to promote UOR kinetics.

This interpretation aligns with previous studies—for example, Au/ZnO systems forming O-SMSI showed better CO oxidation performance than those with reductive SMSI (R-SMSI), where charge transfer occurs in the opposite direction.[43]

Similar behavior is observed in our Ni/GZO catalysts. Calculations of Schottky barrier height (E_{SBH}) values (Table S3) indicate that the extent of electron transfer from Ni to the oxide follows the order G2ZO > G4ZO > G6ZO. This corresponds to stronger O-SMSI formation in Ni/G2ZO, which also shows the highest catalytic performance among the tested compositions. XPS analysis supports this conclusion: the Ni^{2+} $2p_{3/2}$ peak shift (Fig. S9) increases in the same order (G2ZO > G4ZO > G6ZO), confirming greater electron donation from Ni to the oxide in Ni/G2ZO. Additionally, the intrinsic UOR activity of the oxides themselves (before Ni loading) follows the same order, suggesting that oxide properties also contribute to catalytic performance. However, the charge difference between Ni/G2ZO and Ni/G4ZO after Ni deposition is over 12 times larger than that between G2ZO and G4ZO alone. This highlights that the metal/oxide interface, rather than the oxide itself, plays a dominant role in enhancing catalytic activity. In summary, while the intrinsic activity of the oxide support is important, creating maximizing overall catalytic efficiency in UOR.

In contrast, metal/oxide catalysts with Schottky junctions show lower catalytic performance, which can be mainly attributed to the high electrical resistivity of the oxide support. In these systems, limited charge mobility across the interface hinders efficient electron transfer, increasing the overpotential and reducing the overall catalytic efficiency. For example, Ponja et al. reported that the resistivity (ρ) of Ga-doped ZnO varies depending on Ga content: undoped ZnO has a resistivity of 2.14 × 10^{-3} Ω·cm, while values for 1, 5, and 8 at.% Ga-doped ZnO are 1.4 × 10^{-3}, 0.79 × 10^{-3}, and 1.24 × 10^{-3} Ω·cm, respectively.[51] This trend indicates that resistivity increases in the order of 5 > 8 > 1 at.% Ga, and thus, charge transfer becomes more restricted with certain doping levels. Additionally, the secondary phase β-Ga_2O_3, which forms at higher Ga concentrations, has a significantly lower resistivity (5.01 × 10^3 Ω·cm) than ZnO (7.5 × 10^8 Ω·cm).[52,53] As the fraction of β-Ga_2O_3 increases, the overall resistivity of the oxide phase decreases, which helps partially recover the catalytic activity in samples like Ni/G10ZO. This correlates with the observed UOR activity trend of Ni/GZO samples—10% > 8% > 0% Ga doping—as measured by LSV. Therefore, in Schottky junction systems, the catalytic performance is governed less by the intrinsic catalytic properties of the oxide and more by its electrical resistivity. For optimal design, selecting oxide supports with low resistivity is

critical to minimizing charge transfer limitations and improving catalytic output.

The electrochemical durability of different junction types was evaluated by comparing Ni/G2ZO, which forms an Ohmic junction, with Ni/ZO, which forms a Schottky junction. Chronoamperometry results (Fig. 4(i)) showed that when a constant potential of 1.7 V was applied, Ni/G2ZO produced approximately 2.1 times more current than Ni/ZO. This higher current is not only due to the O-SMSI effect but also because G2ZO has lower resistivity than undoped ZnO, allowing more efficient electron transport through the oxide support.

Another factor contributing to the improved performance of Ni/G2ZO is the reverse bias condition. In urea oxidation, electrons are generally transferred from the Ni metal to the ZnO support. In an Ohmic junction, this reverse bias has little effect on conduction. However, in a Schottky junction, it maintains the Schottky barrier and expands the depletion region, making electron tunneling more difficult and thus further restricting current flow.[54,55]

This difference in interfacial behavior also affects long-term stability. Ni/G2ZO maintained its high current output for up to 12 hours, while Ni/ZO began to degrade after 6.1 hours (Fig 4(i)). This can be explained by the nature of each junction. Ohmic junctions allow free, bidirectional electron flow due to the absence of a significant potential barrier, resulting in low resistance. In contrast, Schottky junctions impose an energy barrier at the metal/oxide interface, which limits charge transfer and creates higher interfacial resistance.[56]

Over time, this resistance becomes a critical source of instability at the metal/oxide interface. A study by Lord et al. investigated the long-term structural stability of Schottky and Ohmic junctions using Au catalyst/ZnO nanowire systems.[57] In this system, the researchers controlled the junction type by modifying the edge-tunneling effect—a quantum mechanical phenomenon where electrons preferentially tunnel through thinner or structurally favorable regions at the edge of the metal–semiconductor interface.[58] When enhanced edge-tunneling paths were present—created, for example, by architectural modifications or etching during fabrication—the system exhibited Ohmic behavior, characterized by stable and efficient charge transfer. However, when edge-tunneling paths were absent and current had to pass through the central contact region with higher resistivity, the system reverted to Schottky behavior. Under such conditions, the high resistance contact restricted charge flow and caused significant electrical stress at the interface. Through aberration-corrected scanning transmission electron microscopy (ac-STEM), Lord et al. observed that this electrical stress led to the formation of atomic-scale defects near the Au–ZnO interface edge, particularly in systems with Schottky behavior.[59] These defects disrupted the uniformity of the interface, acted as scattering centers for charge carriers, and reduced overall conductivity. As the system operated under constant bias, the resistivity further increased, accelerating defect growth and leading to faster degradation of catalytic performance.

Similarly, Mosbacker et al. observed that in Ta/ZnO systems with Schottky junctions, annealing led to the formation of oxide-blocking layers at the interface.[60] These layers, caused by exothermic metal oxidation, severely limited current flow. Given that Ni behaves similarly to Ta in the context that Ni oxidizes exothermically ($E^0 = -0.23$ V) and has a lower oxidation potential than noble metals like Au, similar oxide growth and blocking behavior can be expected in Ni/ZnO systems. As temperature rises during operation—due to resistive Joule heating at the Schottky interface—oxygen diffusion increases. This promotes the gradual formation of oxygen-deficient ZnO and oxygen-rich Ni layers, increasing the interfacial resistivity and causing further heating. This positive feedback accelerates the formation of defects and leads to faster performance degradation.

These observations suggest that the gradual formation of atomic-scale defects near the metal/oxide interface—driven by Joule heating and oxygen migration—is a direct consequence of the high interfacial resistivity characteristic of Schottky junctions. This highlights the critical role of junction type not only in determining initial catalytic activity but also in governing long-term operational stability under electrochemical conditions.

4. Conclusions

This study confirms that the type of junction formed at the metal/oxide interface plays a decisive role in both the activity and durability of Ni/ZnO-based catalysts for UOR. By systematically adjusting the Ga doping concentration, we observed a transition from Schottky to Ohmic junctions at 2 at.% Ga, followed by a reversion to Schottky-type behavior at 8 at.% due to the emergence of a secondary Ga_2O_3 phase. Catalysts forming Ohmic junctions—namely Ni/G2ZO, Ni/G4ZO, and Ni/G6ZO—exhibited up to 170% higher current generation and 6% lower overpotential compared to those with Schottky junctions. This improvement was attributed to directional electron transfer from Ni to the oxide, producing a positively charged Ni surface and a negatively charged oxide surface, a signature of oxidative strong metal–support interaction (O-SMSI). Importantly, the two types of junctions were found to be governed by distinct performance-determining factors. In Ohmic junctions, the low interfacial resistance enabled the intrinsic catalytic activity of the oxide to be fully expressed, making the oxide's inherent reactivity the dominant contributor to overall performance. In contrast, Schottky junctions imposed a potential barrier that limited charge mobility, rendering the oxide's electrical resistivity the primary factor controlling catalytic efficiency. Electrochemical durability tests reinforced these findings. Ni/G2ZO, an Ohmic system, sustained high current output for up to 12 hours, whereas Ni/ZO, a Schottky system, showed significant performance degradation after only 6.1 hours. The enhanced stability of Ohmic junctions was attributed to their lower interfacial resistance, which minimized Joule heating and suppressed defect formation at the metal–oxide interface. Overall, these results highlight the critical role of junction engineering in electrocatalyst design. Constructing Ohmic junctions not only maximizes catalytic activity by utilizing the oxide's intrinsic reactivity but also improves long-term

durability by ensuring stable charge transport. This strategy offers valuable insights for the development of high-performance catalysts for UOR and related electrochemical applications.

Author contributions

Yoo Lim Cha: Conceptualization, Data curation, Formal analysis, Investigation, Methodology, Project administration, Resources, Validation, Visualization, Writing – original draft, review & editing. Shuai Wu: Investigation, Methodology, Resources, Validation. Md Sabbir Hossen Bijoy: Formal analysis, Resources, Methodology. Seyed Morteza Taghavi Kouzehkanan: Formal analysis, Resources, Methodology. Wonhyeong Kim: Formal analysis, Resources, Methodology. Pengyu Chen: Data curation, Formal analysis. Tae-Sik Oh: Data curation, Formal analysis. Fariborz Kargar: Data curation, Formal analysis. Sun Hee Kim: supervision, project administration. Dong-Joo Kim: supervision, project administration

Conflicts of interest

There are no conflicts to declare.

Data availability

The data supporting this article have been included as part of the ESI.†

Acknowledgements

The authors acknowledge the financial support of Incheon National University Research Grant in 2024 and the NSF CAREER CBET-1943302.

Notes and references

1 A. T. Miller, B. L. Hassler and G. G. Botte, *J Appl Electrochem*, 2012, **42**, 925–934.
2 W. Simka, J. Piotrowski and G. Nawrat, *Electrochimica Acta*, 2007, **52**, 5696–5703.
3 W. Yan, D. Wang and G. G. Botte, *Electrochimica Acta*, 2012, **61**, 25–30.
4 W. Simka, J. Piotrowski, A. Robak and G. Nawrat, *J Appl Electrochem*, 2009, **39**, 1137–1143.
5 S. Shen, M. Li, B. Li and Z. Zhao, *Environ Sci Pollut Res*, 2014, **21**, 12563–12568.
6 A. M. Bernhard, D. Peitz, M. Elsener, A. Wokaun and O. Kröcher, *Applied Catalysis B: Environmental*, 2012, **115–116**, 129–137.
7 P. Basumatary, D. Konwar and Y. S. Yoon, *Electrochimica Acta*, 2018, **261**, 78–85.
8 A. V. Ananiev, J.-C. Broudic and P. Brossard, *Applied Catalysis B: Environmental*, 2003, **45**, 189–196.
9 G. Kumar, E. Nikolla, S. Linic, J. W. Medlin and M. J. Janik, *ACS Catal.*, 2018, **8**, 3202–3208.
10 A. Holewinski, H. Xin, E. Nikolla and S. Linic, *Current Opinion in Chemical Engineering*, 2013, **2**, 312–319.
11 J. Yoon, E. Lee, D. Lee, T.-S. Oh, Y. S. Yoon and D.-J. Kim, *J. Electrochem. Soc.*, 2017, **164**, B558.
12 J. Yoon, D. Lee, E. Lee, Y. S. Yoon and D.-J. Kim, *Electroanalysis*, 2019, **31**, 17–21.
13 X. Li, Q. Dong, F. Li, Q. Zhu, Q. Tian, L. Tian, Y. Zhu, B. Pan, M. Padervand and C. Wang, *Applied Catalysis B: Environmental*, 2024, **340**, 123238.
14 A. T. Sivagurunathan, T. Kavinkumar and D.-H. Kim, *Journal of Materials Chemistry A*, 2024, **12**, 32117–32131.
15 J.-J. Zhang, H. Su, H.-H. Wang, Z.-H. Xue, B. Zhang, X. Wei, X.-H. Li, S.-I. Hirano and J.-S. Chen, *Nano Energy*, 2017, **39**, 321–327.
16 J. Hölzl and F. K. Schulte, in *Solid Surface Physics*, eds. J. Hölzl, F. K. Schulte and H. Wagner, Springer, Berlin, Heidelberg, 1979, pp. 1–150.
17 N. D. Lang and W. Kohn, *Phys. Rev. B*, 1971, **3**, 1215–1223.
18 H. B. Michaelson, *Journal of Applied Physics*, 1977, **48**, 4729–4733.
19 V. Vedharathinam and G. G. Botte, *Electrochimica Acta*, 2012, **81**, 292–300.
20 F. Guo, K. Ye, K. Cheng, G. Wang and D. Cao, *Journal of Power Sources*, 2015, **278**, 562–568.
21 S. S. Wilson, J. P. Bosco, Y. Tolstova, D. O. Scanlon, G. W. Watson and H. A. Atwater, *Energy & Environmental Science*, 2014, **7**, 3606–3610.
22 D. Li, X. Jiang, Y. Zhang, B. Zhang and C. Pan, *Journal of Materials Research*, 2013, **28**, 507–512.
23 S. Barthwal and N. B. Singh, *Materials Today: Proceedings*, 2020, **29**, 749–752.
24 K. B. Babitha, P. S. Soorya, A. Peer Mohamed, R. B. Rakhi and S. Ananthakumar, *Mater. Adv.*, 2020, **1**, 1939–1951.
25 Y.-Q. Li, K. Yong, H.-M. Xiao, W.-J. Ma, G.-L. Zhang and S.-Y. Fu, *Materials Letters*, 2010, **64**, 1735–1737.
26 E. Muchuweni, T. S. Sathiaraj and H. Nyakotyo, *Ceramics International*, 2016, **42**, 10066–10070.
27 H.-S. Hong and G.-S. Chung, *Sensors and Actuators B: Chemical*, 2010, **150**, 681–685.
28 A. Alexandrov, M. Zvaigzne, D. Lypenko, I. Nabiev and P. Samokhvalov, *Scientific Reports*, 2020, **10**, 7496.
29 G. C. Park, S. M. Hwang, J. H. Lim and J. Joo, *Nanoscale*, 2014, **6**, 1840–1847.
30 S.-J. Young, C.-L. Chiou, Y.-H. Liu and L.-W. Ji, *Inventions*, 2016, **1**, 3.
31 P. Sathish, N. Dineshbabu, K. Ravichandran, T. Arun, P. Karuppasamy, M. SenthilPandian and P. Ramasamy, *Ceramics International*, 2021, **47**, 27934–27941.
32 Y.-S. Lee, Y.-C. Peng, J.-H. Lu, Y.-R. Zhu and H.-C. Wu, *Thin Solid Films*, 2014, **570**, 464–470.
33 T. Shinagawa, K. Shibata, O. Shimomura, M. Chigane, R. Nomura and M. Izaki, *Journal of Materials Chemistry C*, 2014, **2**, 2908–2917.
34 Y.-F. Yao, K.-P. Chou, H.-H. Lin, C.-C. Chen, Y.-W. Kiang and C. C. Yang, *ACS Appl. Mater. Interfaces*, 2018, **10**, 40764–40772.
35 K. Govender, D. S. Boyle, P. B. Kenway and P. O'Brien, *Journal of Materials Chemistry*, 2004, **14**, 2575–2591.
36 J. H. Lim, S. M. Lee, H.-S. Kim, H. Y. Kim, J. Park, S.-B. Jung, G. C. Park, J. Kim and J. Joo, *Sci Rep*, 2017, **7**, 41992.
37 X. Zhang, J. Qin, Y. Xue, P. Yu, B. Zhang, L. Wang and R. Liu, *Sci Rep*, 2014, **4**, 4596.
38 M. Honda, T. Goto, T. Owashi, A. G. Rozhin, S. Yamaguchi, T. Ito and S. A. Kulinich, *Physical Chemistry Chemical Physics*, 2016, **18**, 23628–23637.
39 Y. L. Cha, J.-H. Jo, D.-J. Kim and S. H. Kim, *Nanomaterials*, 2022, **12**, 2060.

40 A. R. Bhapkar, M. Geetha, D. Jaspal, K. Gheisari, M. Laad, J.-J. Cabibihan, K. K. Sadasivuni and S. Bhame, *Appl Nanosci*, 2023, **13**, 5777–5793.
41 Y. S. Chen, J. F. Kang, B. Chen, B. Gao, L. F. Liu, X. Y. Liu, Y. Y. Wang, L. Wu, H. Y. Yu, J. Y. Wang, Q. Chen and E. G. Wang, *J. Phys. D: Appl. Phys.*, 2012, **45**, 065303.
42 X. Hao, Y. Fan, W. Deng and Z. Jin, *Carbon*, 2024, **218**, 118752.
43 X. Liu, M.-H. Liu, Y.-C. Luo, C.-Y. Mou, S. D. Lin, H. Cheng, J.-M. Chen, J.-F. Lee and T.-S. Lin, *J. Am. Chem. Soc.*, 2012, **134**, 10251–10258.
44 S. Prucnal, K. Gao, S. Zhou, J. Wu, H. Cai, O. D. Gordan, D. R. T. Zahn, G. Larkin, M. Helm and W. Skorupa, *Applied Physics Letters*, 2014, **105**, 221903.
45 S. M. Tavender, S. A. Johnson, D. Balsom, A. W. Parker and R. H. Bisby, *Laser Chemistry*, 1999, **19**, 056589.
46 O. Reckeweg, A. Schulz and F. J. DiSalvo, *Zeitschrift für Naturforschung B*, 2020, **75**, 129–133.
47 M. Suzuki, S. Koizumi, M. Katagiri, T. Ono, N. Sakuma, H. Yoshida, T. Sakai and S. Uchikoga, *physica status solidi (a)*, 2006, **203**, 3128–3135.
48 M. A. Rahman, M. M. Rahman, A. M. M. T. Karim, M. A. Sattar, M. A. Halim and M. K. R. Khan, *Chinese Journal of Physics*, 2018, **56**, 1781–1788.
49 J. Ma, J. Lin, J. Liu, F. Li, Y. Liu and G. Yang, *Chemical Physics Letters*, 2020, **746**, 137308.
50 W. G. Oldham and A. G. Milnes, *Solid-State Electronics*, 1963, **6**, 121–132.
51 S. D. Ponja, S. Sathasivam, I. P. Parkin and C. J. Carmalt, *Sci Rep*, 2020, **10**, 638.
52 D. Wang, L. He, X. Ma, H. Xiao, Y. Le and J. Ma, *Materials Characterization*, 2020, **165**, 110391.
53 D. L. Raimondi and E. Kay, *Journal of Vacuum Science and Technology*, 1970, **7**, 96–99.
54 J. Li, H. Wang, M. Luo, J. Tang, C. Chen, W. Liu, F. Liu, Y. Sun, J. Han and Y. Zhang, *Solar Energy Materials and Solar Cells*, 2016, **149**, 242–249.
55 S. J. T. Owen and T. L. Tansley, *Journal of Vacuum Science and Technology*, 1976, **13**, 954–960.
56 L. J. Brillson and Y. Lu, *Journal of Applied Physics*, 2011, **109**, 121301.
57 A. M. Lord, Q. M. Ramasse, D. M. Kepaptsoglou, P. Periwal, F. M. Ross and S. P. Wilks, *Nano Lett.*, 2017, **17**, 6626–6636.
58 A. M. Lord, V. Consonni, T. Cossuet, F. Donatini and S. P. Wilks, *ACS Appl. Mater. Interfaces*, 2020, **12**, 13217–13228.
59 J. R. Wang, D. H. Zhu, J. L. Chen and B. C. Pan, *Journal of Nuclear Materials*, 2023, **581**, 154418.
60 H. L. Mosbacker, C. Zgrabik, M. J. Hetzer, A. Swain, D. C. Look, G. Cantwell, J. Zhang, J. J. Song and L. J. Brillson, *Applied Physics Letters*, 2007, **91**, 072102.

Data availability statement

The data supporting this article have been included as part of the ESI.†